Growth and Characterization of Cubic InGaN and InGaN/GaN Quantum Wells

Dem Department Physik

der Universität Paderborn

zur Erlangung des akademischen Grades eines

Doktors der Naturwissenschaften

vorgelegte

Dissertation

von

Shunfeng Li

Paderborn, Juni 2005

Abstract

Due to the high symmetry of the cubic III-nitride crystal unit, physical properties of the cubic III-nitrides were predicted theoretically, which are superior to those of their thermodynamically stable hexagonal counterparts. High quality c-InGaN layers and quantum structures, which form the active layers of optoelectronic devices are indispensable for realization of the highly efficient blue and green emission from c-III nitride based LEDs and Laser diodes. In this thesis, the epitaxy of high quality c-InGaN layers and InGaN/GaN wells (QWs) is optimized and the influence of various growth parameters on their structural and optical properties is investigated.

The Molecular Beam Epitaxy (MBE) of c-GaN, as well as efforts to grow thick c-GaN layers by Metal Organic Chemical Vapor Deposition (MOCVD) on top of MBE grown c-GaN buffer layers are briefly introduced. The influence of the indium and gallium fluxes on the MBE of high quality c-InGaN is studied extensively. Indium is observed to incorporate into the c-InGaN films only when the gallium flux is reduced significantly below the value needed for stoichiometric c-GaN growth. A decrease of the surface roughness of the InGaN layers and an increase of their photoluminescence intensity per unit thickness at the transition from metal-flux limited to active nitrogen-limited growth is observed. A pronounced reduction of the growth rate is observed when indium is involved in the growth. In order to explain these effects, it is supposed that excess indium atoms present on the InGaN surface due In segregation are the reason for the growth rate reduction. Based on these investigations, a recipe for the growth of high quality c-InGaN is proposed. High-resolution X-ray diffraction and Raman measurements show that InGaN layers grown on 3C-SiC substrates have better structural quality than those grown on GaAs substrates. Photoluminescence excitation (PLE) spectroscopy and photoluminescence (PL) measurements reveal that the emission from c-InGaN layers originates from highly localized structures in these layers. The room temperature PL spectra of c-$In_xGa_{1-x}N$ grown on 3C-SiC substrates are dominated by two preferential peaks at around 2.4 eV and 2.6 eV with a slight red shift with increasing x in the range of $0<x<0.2$. Depth resolved cathodoluminescence and PLE demonstrate the existence of In-rich phases, which are found by transmission electron microscopy (TEM) to be oriented along the growth direction. By thermal annealing experiments, stability of these inclusions in the c-InGaN layer is investigated, revealing that they are stable even at annealing temperatures above the growth temperatures, which allows some conclusions on the mechanism of their formation.

The PL emission intensity from c- InGaN/GaN single quantum wells is found to increase with increasing well thickness, which proves the absence of polarization fields in cubic III-nitrides. The InGaN/GaN MQWs were grown with a growth interruption after the InGaN well growth allowing excess In atoms to evaporate yielding sharp InGaN/GaN interfaces. With this growth procedure, highly efficient c-InGaN/GaN MQWs with 515nm room temperature PL emission (FWHM 240meV) and clear superlattice peaks in X-ray diffraction patterns have been realized. Finally, the effect of a c-AlGaN/GaN Bragg-mirror micro-cavity on the 520nm green emission from c-InGaN/GaN MQWs has been demonstrated for the first time.

List of Figures

Figure 2.1 Schematic drawing of MBE system 8
Figure 2.2 Ga atom flux versus the corresponding Ga BEP 9
Figure 2.3 In atomic flux versus the corresponding In BEP 10
Figure 2.4 Schematic drawing of the Philips X´Pert MRD 10
Figure 2.5 X-ray scattering geometry 11
Figure 2.6 Reciprocal space map for Bragg reflection measurements 12
Figure 2.7 Schematic drawing of photoluminescence setup 14
Figure 2.8 Schematic drawing of cathodoluminescence setup 15
Figure 2.9 Schematic drawing of photoluminescence excitation setup 16

Figure 3.1 Ga/N ratio versus substrate temperature for c-GaN growth 21
Figure 3.2 Typical HRXRD linescan on cubic GaN samples grown on GaAs and 3C-SiC substrates 22
Figure 3.3 Room temperature PL spectra of GaN layers grown on GaAs and 3C-SiC substrates 23
Figure 3.4 XRD rocking curves on c-GaN layers 24
Figure 3.5 XRD rocking curve on GaN (002) reflexes of MOCVD GaN thick buffer layer and layer after MBE GaN growth on it 25

Figure 4.1 Schematic drawing of ordered and disordered phases 29
Figure 4.2 Binodal (solid) and spinodal (dashed) curves for the $Ga_{1-x}In_xN$ system 30
Figure 4.3 Spontaneous and piezoelectric polarization field in the III-nitride and the crystal configuration 32
Figure 4.4 Band profile and carriers distribution in cubic and hexagonal InGaN/GaN quantum well 32
Figure 4.5 Reaction pathways for the deposition of In-based nitride compounds 35
Figure 4.6 RHEED patterns of c-InGaN layers 37
Figure 4.7 Transition time interval of surface reconstruction after shuttering the metal flux dependence on In flux 38
Figure 4.8 XRD ω-2θ scans of the (002)-Bragg reflex of c-InGaN/GaN/SiC samples 39
Figure 4.9 The RMS surface roughness of c-InGaN versus indium flux 40
Figure 4.10 Indium mole fraction of InGaN layers as a function of the In flux 41
Figure 4.11 a) Room temperature PL spectra of c-InGaN. b) PL peak energy and PL intensity per unit thickness as a function of the indium flux 42
Figure 4.12 Indium molar fraction of c-InGaN layers as a function of the gallium flux 43
Figure 4.13 Indium molar fraction of c-InGaN layers grown on GaAs substrate as a function of the gallium flux 44
Figure 4.14 Normalized growth rate of InGaN to GaN versus In mole fraction x 45
Figure 4.15 Schematic drawing InGaN surface reaction process and surface morphology on InGaN (001) surface 46
Figure 4.16 The $20 \times 20\ \mu m^2$ typical AFM picture on surface of c-InGaN 49
Figure 4.17 The $20 \times 20\ \mu m^2$ typical AFM picture on surface of GaN 49
Figure 4.18 XRD (-1-13) and (002) RSM around GaN and InGaN reflexes 50
Figure 4.19 XRD (-1-13) RSM of InGaN grown on 3C-SiC substrate and GaAs substrates 51
Figure 4.20 The calculated critical thickness of c-$In_xGa_{1-x}N$ on GaN versus the In mole fraction x 52

Figure 4.21 HRXRD -2 scan on InGaN/GaN samples with different In mole fraction using GaAs substrate ... 54
Figure 4.22 HRXRD -2 scan on InGaN/GaN samples with different In mole fraction using 3C-SiC substrates ... 54
Figure 4.23 Relation between the ratio of the FWHM difference of InGaN and GaN to the FWHM of GaN and the indium mole fraction ... 55
Figure 4.24 Transmission electron microscopy on InGaNDH1112 ... 56
Figure 4.25 Raman spectra of c-InGaN ... 58
Figure 4.26 Typical Raman spectra from c-InGaN using 3C-SiC substrate #1149 and GaAs substrate #868 ... 59
Figure 4.27 InGaN LO phonon frequency versus In mole fraction ... 59
Figure 4.28 Low temperature PL spectra on c-InGaN samples ... 63
Figure 4.29 a) 7K PL measurement on $In_{0.13}Ga_{0.87}N$#1154 by various light wavelength excitation from the lamp. B) 7K PL at excitation light of 2.54eV and PLE measurement ... 63
Figure 4.30 Low temperature (7K) PL spectra and PLE spectra ... 64
Figure 4.31 PLE measurement on $In_xGa_{1-x}N$ with different x at 7K ... 65
Figure 4.32 InGaN band gap versus In mole fraction x ... 67
Figure 4.33 Room temperature PL spectra from $In_xGa_{1-x}N$ with different x ... 68
Figure 4.34 PL peak energy and band gap of $In_xGa_{1-x}N$ versus In mole fraction ... 69
Figure 4.35 Temperature dependent PL spectra from $In_{0.06}Ga_{0.94}N$ ... 70
Figure 4.36 PL peak energy versus temperature from the $In_{0.06}Ga_{0.94}N$ ... 71
Figure 4.37 PL intensity of the 2.4 eV and 2.6 eV peaks . versus 1000/T ... 72
Figure 4.38 a) PL spectra of $In_{0.13}Ga_{0.87}N$ DH#1162 from 5K to 300K, b) PL peak energy versus 1000/T, the arrenhius plot, c) PL peak energy versus temperature ... 73
Figure 4.39 Depth resolved CL spectra on $In_{0.05}Ga_{0.95}N$ #868 ... 74
Figure 4.40 Schematical drawing of electron distribution in the InGaN samples ... 75
Figure 4.41 CL emission peaks energy versus penetration depth ... 75
Figure 4.42 CL intensity ratio versus the electron penetration depth ... 76
Fig.4.43 distribution of the electron in InGaNDH#1231 at various voltages ... 76
Figure 4.44 Room temperature depth resolved CL spectra from InGaNDH#1231 ... 77
Figure 4.45 CL emission peak energy versus penetration depth ... 78
Figure 4.46 Annealing temperature on InGaN sample versus keeping time ... 79
Figure 4.47 (-1-13) Reciprocal space maps on annealed sample InGaNDH#1124 ... 80
Figure 4.48 Room temperature PL spectra before and after thermal annealing ... 81

Figure 5.1 Finite depth quantum well conduction band profile ... 83
Figure 5.2 Schematicall drawing on InGaN/GaN SQW and MQW samples ... 85
Figure 5.3 Room temperature PL spectra of InGaN/GaN single quantum well with different well thickness grown on GaAs substrates ... 86
Figure 5.4 Room temperature PL spectra of InGaN/GaN single quantum well grown on 3C-SiC substrates ... 86
Figure 5.5 Calculated and experimental transition energy versus with well thickness ... 87
Figure 5.6 Integrated PL intensity ratio of the InGaN SQW samples versus the InGaN well thickness ... 88
Figure 5.7 RHEED pattern of the InGaN growth, a) before growth interruption, b) after growth interruption ... 89
Figure 5.8 HRXRD (-1-13) reciprocal space map on InGaN/GaN MQWs ... 90
Figure 5.9 HRXRD (002) -2 scans of a) type A sample, b) type B ... 90
Figure 5.10 Room temperature PL spectra of the two different type of samples ... 91
Figure 5.11 The -2 of (002) and (004) reflex of the InGaNMQW1219 ... 92
Figure 5.12 a) XRD patterns of InGaN/GaN MQWs#1219 ... 93

Figure 5.13 300K and 2K PL spectra of $In_{0.12}Ga_{0.88}N$ MQW#1212 94
Figure 5.14 Room temperature and 2K PL spectra of $In_{0.13}Ga_{0.87}N$MQW1213 95
Figure 5.15 Room temperature and 2K PL spectra of $In_{0.13}Ga_{0.87}N$MQW1218 96
Figure 5.16 In mole fraction and thickness of the InGaN wells versus different growth time 97
Figure 5.17 PL peak energy versus well thickness 97
Figure 5.18 Room temperature PL spectra of $In_{0.07}Ga_{0.93}N$SQW#1111 and $In_{0.12}Ga_{0.88}N$ MQW#1212 98
Figure 5.19 Schematic layer sequence of nitride based RCLED 100
Figure 5.20 Schematic drawing of cubic AlGaN/GaN DBR 102
Figure 5.21 Reflectivity measurement and simulation results on the 15folds c-AlGaN/GaN DBR 102
Figure 5.22 The resonant cavity structure without top mirror 103
Figure 5.23 Angular dependent room temperature PL spectra of resonant cavity structure 104
Figure 5.24 Schematic drawing of the angular dependent PL measurement 104

List of Tables

Table 1.1 Basic parameters of hexagonal and cubic GaN 5
Table 2.1 The atomic weight, atomic number and material density of GaN and InN 15
Table 3.1 Summary of substrates for hexagonal and cubic growth and its results 20
Table 4.1 Basic physic and parameter of hexagonal and cubic InN 28
Table 4.2 Information of the c-InGaN samples for varying indium and Gallium flux.................36
Table 4.3 InGaN samples with different Ga flux by using GaAs substrates................................44
Table 4.4 Samples information of c-InGaN for characterization 48

Contents

1 Introduction **3**

2 Growth and characterization methods **7**
2.1 Growth methods 7
2.1.1 Molecular beam epitaxy (MBE) 7
2.1.2 Metalorganic chemical vapor deposition (MOCVD) 9
2.2 X-ray diffraction 10
2.3 Luminescence 12
2.3.1 Photoluminescence 13
2.3.2 Cathodoluminescence 14
2.4 Photoluminescence excitation spectroscopy 16

3 **Cubic GaN growth** **19**
3.1 Selection of substrates for cubic GaN growth 19
3.2 Brief introduction of cubic GaN growth 19
3.2.1 Diagram of surface reconstruction transition in cubic GaN growth 19
3.2.2 Structural quality of c-GaN grown on 3C-SiC and GaAs substrates 21
3.2.3 MOCVD growth of c-GaN 23
3.2.4 MBE growth of c-GaN on MOCVD thick c-GaN layer 24

4 Growth and Characterization of cubic InGaN **27**
4.1 Review of InGaN growth 27
4.2 Some remarkable issues of c-InGaN 29
4.2.1 Alloy order and disorder 29
4.2.2 Phase separation 30
4.2.3 In segregation 30
4.2.4 Polarization fields in III-nitirdes 31
4.2.5 Stokes like shift 33
4.2.6 InGaN bandgap bowing and InN bandgap 34
4.3 Competitive processes in InGaN growth 34
4.4 Cubic InGaN growth 35
4.4.1 C-InGaN growth with varying In flux 37
4.4.2 C-InGaN growth with different Ga flux 41
4.4.3 Discussion and modeling of c-InGaN growth 45
4.4.4 Determination of c-InGaN growth parameters 46
4.5 Surface properties 48

4.6 Structural properties 50
4.6.1 Determination of the strain and In mole fraction in c-InGaN 50
4.6.2 Critical thickness 51
4.6.3 High resolution X-ray diffraction linescan of c-InGaN 53
4.6.4 Transmission electron microscopy results 56
4.6.5 Raman scattering measurements 57
4.7 Optical properties of c-InGaN 61
4.7.1 Photoluminescence excitation spectroscopy measurement on c-InGaN 61
4.7.2 Band gap determination of c-InGaN 66
4.7.3 Photoluminescence measurement on c-InGaN 67
4.7.4 Depth-resolved cathodoluminescence measurement 73
4.8 Thermal annealing results of c-InGaN 78

5 Growth and properties of c-InGaN/GaN quantum wells and application 83
5.1 Quantum size effect in finite depth quantum well 83
5.2 Sample description 85
5.3 Optical properties of single quantum well 85
5.4 Photoluminescence intensity changing with well thickness 88
5.5 Cubic InGaN/GaN multiple quantum wells 89
5.5.1 Growth interruption in c-InGaN/GaN quantum wells growth 89
5.5.2 Simulation of X-ray diffraction pattern 91
5.5.3 Photoluminescence of InGaN/GaN multiple quantum wells 94
5.5.4 InGaN/GaN multiple quantum wells with different well growth time 96
5.5.5 Comparison of single and multiple quantum wells 98
5.6 Application of c-InGaN multiple quantum wells in a resonant cavity structure 99
5.6.1 Resonant cavity light emitting diodes 99
5.6.2 AlGaN/GaN distributed Bragg reflector 101
5.6.3 Combined structure of c-InGaN/GaN multiple quantum wells and c-AlGaN/GaN distributed Bragg reflectors 103

6 Conclusions 107

Bibliography 111

Publications

Acknowledgements

Curriculum Vitae

1. Introduction

In the last decade, III-nitrides have emerged to be new promising materials for optoelectronic and electronic applications [1,2]. Due to their superior physical and chemical properties, III-nitride, i.e. GaN and its alloys have been successfully applied in new short wavelength emitting optoelectronic devices.

The emission wavelength of InN and GaN alloy covers the whole visible light range from ultraviolet to infrared [3]. Therefore, the alloy can be used as the active region of the visible light emitting diode and laser diode, which have extensive commercial applications, such as full-color screen, reading and writing on high volume digital versatile disk (DVD) and optical communication. One of the ambitious goals of scientists is to replace the conventional light sources by the highly efficient III-nitride based solid-state light sources. Up to now, a white LED with a luminous efficiency close to 80lm/W has already been demonstrated in laboratory [4], which is much higher than the conventional incandescent lamp, about 7-20lm/W. White LEDs are believed to have the potential for the luminous efficiencies exceeding 300lm/W [5]. Realization of GaN based LED as domestic luminescent light source is expected within a few years of the future. If it is done, huge amounts of energy consumption will be conserved due to its high luminous efficiency. In nitride based laser diodes application, the new, so-called “Blue ray” DVD standard has been established and will be launched later this year, 2005.

For the electronic devices, benefiting from its high melting point temperature, high breakdown voltage, GaN is believed to be suitable in high power, high frequency devices application. Due to the excellent chemical inertness and mechanical properties of III nitrides, GaN based electronic devices are suitable to work in hostile environment, for example, strong caustic environments and the outer space. The high electron mobility transistors (HEMT) [6,7] and field effect transistors (FET) [8,9] have been realized with the materials of AlGaN/GaN.

The research on GaN started in the early twenties of last century. In 1928, the first GaN powder was synthesized by Johnson through the reaction of metallic Ga and NH_3[10]. In 60’s to 70’s, more attentions were put into the research on GaN synthesis and physical properties [11]. The first GaN based device was Zn doped metal-insulating-semiconductor (MIS) light emitting diode fabricated by Pankove et al in 1971[12]. This work was based upon GaN doped with zinc and using indium contacts. It emitted at 475nm under working voltage of 60-100 Volts with very low efficiency.

The invention and application of new crystal synthesis facilities in 70’s and 80’s such as metalorganic chemical vapor deposition (MOCVD) and molecular beam epitaxy (MBE) had boosted the development of GaN research. However, quality of the III-nitride layers was still not satisfactory to the requirement of the devices. In 1986,

Amano et al[13] suggested a two steps growth procedure to improve the quality of the GaN layer by inserting a low temperature AlN nucleation layer prior to the GaN growth. Nakamura et al[14] found that the GaN low temperature nucleation layer worked even better in the high quality GaN layer growth. After this breakthrough, the GaN quality was dramatically improved, which built a basis for the realization of GaN based device.

The highly efficient GaN based devices came to birth only after solving the P type doping problem. Magnesium (Mg) is the most widely used acceptor in p type doping of GaN. Amano et al[15] found that Mg atoms were activated by the low energy electrons irradiation when they used cathodoluminescence to investigate the Mg doped GaN. In 1991, Akasaki et al[16] succeeded in the first p-n homojunction blue LED with good turn-on characteristic using the treatment of low energy electron beam irradiation (LEEBI) on the Mg doped samples. In 1992, Nakamura[17] obtained the p type doping of GaN simply by annealing the as-grown Mg-doped GaN samples at 700°C-800°C in a N_2 atmosphere. The emission wavelength of this LED was 430nm with forward voltage of 4V at 20mA[18]. Nakamura suggested that the Mg atoms could be compensated by hydrogen atoms to a complex as whole in the MOCVD growth. Annealing can break these complexes and activate the Mg atoms to be acceptors. The Mg doped GaN layer grown by MBE shows p type without any post growth treatment. Now, the hole concentrations in Mg doped p type GaN have reached to an order of $10^{18}/cm^3$ [19,20]. This result paved the road for further laser diode application.

In 1997, Nakamura reported the first continuous wave InGaN/GaN multiple quantum wells blue laser diode with life time of 20-30min[21,22]. At end of 1997, the lifetime of Nakamura's laser diode had been increased to 10000 hours [23]. Up to Now, several other groups or companies have also fabricated the InGaN based laser diode using sapphire, GaN epitaxial lateral overgrowth (ELOG) template or SiC substrates [24,25].

Most of the GaN based devices are fabricated based on hexagonal (wurtzite) GaN. However, GaN can also crystallize in metastable cubic configuration (zinc-blende). Work on cubic III-nitrides is motivated by the potential advantages that these materials would offer for (opto-) electronic applications, compared to the commonly employed hexagonal nitrides, once they can be synthesized in sufficiently high quality, listed in the following:

1. Zinc-blende structure is a centro-symmetry structure. Thus no polarization exists in the cubic modification, unlike the hexagonal configuration [26].
2. A higher saturated electron drift velocity has been predicted [27] for cubic nitrides as a result of the reduced phonon scattering rate due to the higher degree of crystal symmetry.
3. A smaller electron effective mass has been reported for c-GaN [28] and a better amenability to p-type doping as well as a lower hole mass are to be expected [29].
4. Output facets of lasers can be obtained by simple cleavage in combination with technologically relevant substrates like GaAs, GaP, Si.
5. The cubic GaN has lower band gap than h-GaN. This is a benefit for the In incorporation to get long wavelength visible light emission.

The basic parameters of hexagonal and cubic GaN are shown in the following table.

	Wurtzite GaN	Zinc-blende GaN
Band gap energy	3.39eV 300K[30] 3.47eV 0K[31]	3.23eV 300K [32] 3.299 eV 0K[33]
Lattice constant (300K)	3.189 A(a) 5.186A (c) [31]	4.52 300K [34]
Debye temperature	600K	600K
Optical phonon Energies(300K)	91.2meV [31]	87.3 meV [31]
Infrared refractive Index	2.3 300 K[35]	2.3 300K [31]
Effective electron mass m_e	0.20 m_o 300 K[31]	0.13m_o 300 K[31]
Effective hole masses (heavy) m_{hh}	1.4 m_o [36]	0.84 m_o [37]
Effective hole masses (light)	0.3m_0 [36]	0.16m_o [37]
Thermal expansion coefficient	5.59×10^{-6} $K^{-1,}$ a 3.17×10^{-6} K^{-1} c [38]	
Electron affinity		4.1 eV 300 K [31]
Cohesive energy		8.96 eV (calculated) [39]

Table 1.1 Basic parameters of hexagonal and cubic GaN

Due to the potentially good physical properties of cubic III nitride, researchers are continuously working on growing high quality cubic III nitride [40,41]. However, there are difficulties, which inhibit the development of cubic III nitrides and device application.

1) Lack of proper substrates

Now, for cubic GaN growth, the widely employed substrates are GaAs [42,43] and 3C-SiC [44,45]. The GaAs substrate has too large lattice mismatch to cubic GaN layer (20%) despite the same crystal polarity. The 3C-SiC substrate offers less lattice mismatch to cubic GaN (3.7%). Small lattice mismatch results in low dislocation density in the epitaxial layer. However, 3C-SiC is one poly type of SiC crystals, which is difficult to achieve with high material quality. Yet another critical factor which influences the growth of cubic GaN layers is thermal expansion coefficient difference between the substrate and the c-GaN epilayer. Large thermal expansion coefficient leads to cracks when the samples are cooled down from growth temperature to room temperature, e.g. hexagonal GaN layer grown on Si substrate tends to have cracks [46].

2) Metastability of cubic III- nitrides

The cubic (zinc-blende) phase of III-nitrides is a metastable phase, which makes the high quality cubic material growth difficult. Metastability of cubic GaN demands the lower growth temperature, e.g. about 200°C lower than hexagonal GaN. Low growth temperature in c-GaN leads to insufficient diffusion of the surface adatoms, which may result in inferior structural quality compared to high temperature grown hexagonal

(wurztize) GaN. Investigation on the cubic GaN growth revealed that the MBE growth of cubic GaN has to be performed at metal rich condition [40]. Otherwise, at N-rich condition the hexagonal GaN growth will occur in c-GaN growth. In contrast, hexagonal GaN can be grown at high temperature in both N rich and metal rich conditions.
In device applications, especially optoelectronic devices, InGaN alloy is a necessary material for active region in visible light emission devices. Due to the large lattice constant and binding energy differences between GaN and InN, there are many remarkable phenomena in InGaN, which make high quality InGaN growth quite difficult. Therefore, the investigation on the InGaN growth and properties is very important to realize highly efficient optoelectronic devices.

This thesis reports the work on cubic III-nitride growth, or more specifically, on the growth and characterization of cubic InGaN and c-InGaN/GaN quantum wells. Chapter 2 begins with a description of the growth and characterization methods utilized, followed by a short introduction on the c-GaN growth in Chapter 3. In chapter 4, the growth of c-InGaN layer has been investigated. A recipe for InGaN growth is proposed. Versatile experimental methods, such as X-ray diffraction, transmission electron microscopy, photoluminescence, photoluminescence excitation measurement and cathodoluminescence have been performed to reveal the optical and structural properties of the c-InGaN layer. Chapter 5 mainly includes the work about the c-InGaN/GaN quantum wells. The growth procedure has been optimized. Optical and structural properties are investigated. Application of InGaN/GaN MQWs in a resonant cavity structure has been tested. Finally, the conclusions were made in chapter 6.

2. Growth and characterization methods

This chapter begins with a brief introduction of our growth methods. For in-depth understanding on the semiconductor material, post-growth characterizations are necessary to carry out the optical and structural properties of the semiconductor material. Several characterization methods are described in this chapter.

2.1 Growth methods

The growth methods, which frequently appear in the literature for III-nitrides are molecular beam epitaxy (MBE) [47,48] and metalorganic chemical vapor deposition (MOCVD) [49].

2.1.1 Molecular beam epitaxy (MBE)

MBE is a sophisticated and widely adopted crystal growth method, which has been discussed in many textbook and papers [50]. It is a non-thermodynamic equilibrium growth method, in which the kinetic processes dominate the growth. MBE growth is normally performed with a relatively low growth temperature. Thanks to the high vacuum growth chamber, plenty of in-situ characterization tools such as reflection high energy electron diffraction (RHEED), scanning tunneling microscopy (STM) help to control the growth even with a mono-atomic layer precision and make online characterization without exposure in the air. Thus one can get good interface and sound material quality with MBE growth. Another advantage of MBE growth is that the dissociation efficiency of the N_2 molecule is not influenced by growth temperature, unlike the case of MOCVD growth, which is good for high In concentration InGaN growth.

If not mentioned, all the cubic III-nitride samples in this work were grown by Riber 32 MBE system equipped with an Oxford research CARS25 radio frequency plasma source for activated nitrogen atoms (shown in Fig. 2.1). The effusion cells are mounted onto the growth chamber between 5 to 32 degrees from the horizontal plane. A liquid-nitrogen cooled cryoshroud is used to minimize the background pressure inside the growth chamber. The typical background pressure with cryoshroud on is 10^{-10} mbar. This ensures the low background doping in the semiconductor. The loading of the sample holder is done via a load lock in order to avoid deterioration of the vacuum in the growth chamber.
Six ABN35 standard elemental sources are mounted onto the MBE growth chamber such that their axes converge on the center of the substrate in the growth position. Five

ports are occupied by Ga, Al, In, Si, Mg and C sources. The beam equivalent pressure of elemental species is measured by a Bayard-Alpert gauge hooked onto the backside of the substrate manipulator. The plasma source from activated nitrogen atoms is water-cooled and operated with an inductively coupled radio frequency (RF) of 13.65 MHz at power of 130-500W. Typical flow rates of the N_2 gas were 0.2-0.7 sccm, resulting in N background pressure of about 2×10^{-5} mbar.

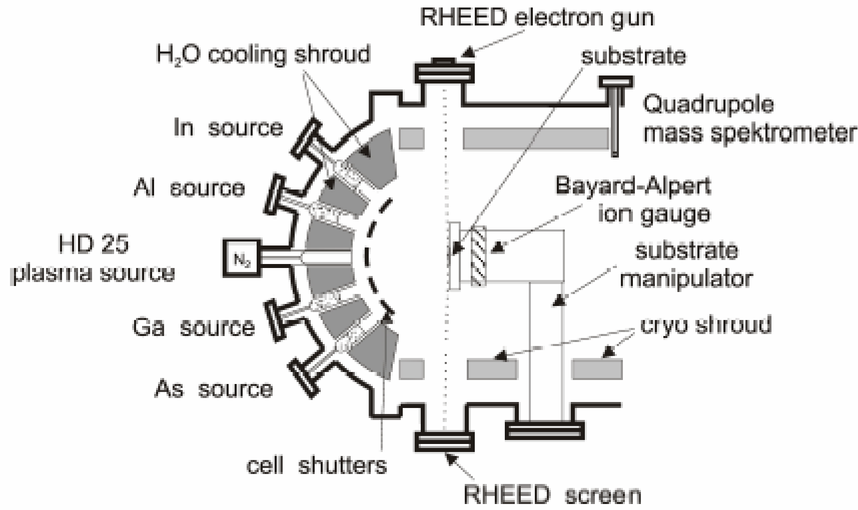

Figure 2.1 Schematic drawing of MBE system.

The *in-situ* RHEED is used to online check the growth. The high energy beam (with energy of 16keV) is scattered by the sample surface to a fluorescence screen. A CCD camera and computer system is employed to capture the graph and make spatial or time-dependent analysis. The rest gas level is monitored by Quadrupole mass spectrometer (QMS). Our QMS can monitor the species up to an atomic mass of 200 amu.

The 3C-SiC or GaAs substrates were cut into small pieces with size of 10×10 mm^2. The same size and substrate preparation were adopted in order to get a high reproducibility of the growth temperature between the different samples. The real temperature of growing surface was calibrated by the indium (In) and lead (Pb) melting point. Via this procedure, the relation between the thermocouple reading temperature and the real sample surface temperature during growth can be established. As a special case for GaAs substrate, the surface temperature can be calibrated also by the surface reconstruction transition from (2×4) to (3×1) at real temperature 660°C when the beam equivalent pressure (BEP) ratio of As to Ga was kept at about 13.

The BEP of metal fluxes were measured by ion gauge. The relation between the flux of the species atoms and their BEP can be expressed by the Knudsen formula:

$$\frac{F}{A} = \frac{N_{Avo} * p}{\sqrt{2 * \pi * M_{mol} * k_B * T}} \tag{2.1}$$

where p is the beam equivalent pressure, F is the flux of atoms, A is the cell aperture. M_{mol} is the mass per mole for the species. T is the source temperature.

The Ga atomic flux can be also measured by the RHEED intensity oscillation of GaAs growth at As rich condition. In this way, the relation of Ga atom flux and its corresponding BEP can be achieved. Figure 2.2 shows the flux of Ga versus its BEP.

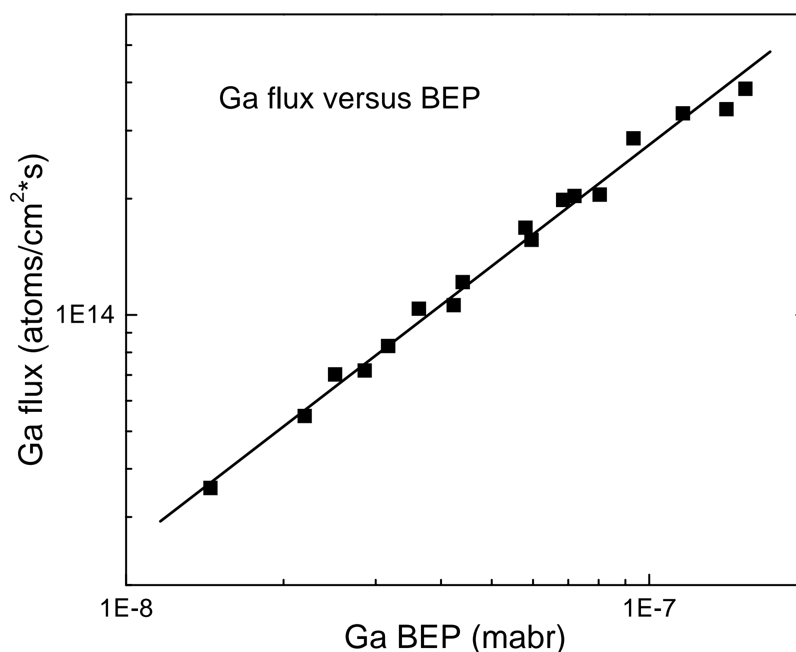

Figure 2.2 Ga atom flux versus its corresponding Ga BEP

Due to the difficulty of observing RHEED intensity oscillation in InGaAs growth, the flux of In atoms has to be calculated in another way. The determination of the atomic flux of In can be achieved by using the BEP of Ga as a calibration point. The relative sensitivity of the Bayard-Alpert ion gauge in the MBE growth chamber is dependent on the atomic number of the species, i.e. Ga, In and Al 1.7, 2.45 and 0.92 [51]. This allows the determination of the elemental flux for In versus its corresponding BEP. The flux of In atoms versus its BEP is plotted Fig 2.3.

In the following, I will use the unit of monolayer/second (ml/s), which is corresponding to the flux (atoms/cm^2/s) in a relation of $1 ml/s = 9.79 \times 10^{14} atoms/s/cm^2$.

2.1.2 Metalorganic chemical vapor deposition (MOCVD)

In MOCVD, the substrate wafer is placed on a graphite susceptor inside a reaction vessel and heated by a radio frequency induction heater. The growth temperature depends on the type of compounds grown, for example, 1000-1100°C for h-GaN growth. Growth occurs in an atmosphere of hydrogen or nitrogen gas at a pressure of 100 to 1000 mbar. The growth precursors decompose via contact with the hot substrate and form epitaxial layers. Group V precursors are NH_3 for GaN while group III are Trimethylgallium (TMGa) or Triethylgallium (TEGa). MOCVD has advantages of

high temperature and high growth rate for GaN growth over MBE. An Aixtron MOCVD equipment was used to perform cubic GaN growth at Linz University. A detailed description of this MOCVD system can be found in the Ph.D thesis of K. Schmidegg [52].

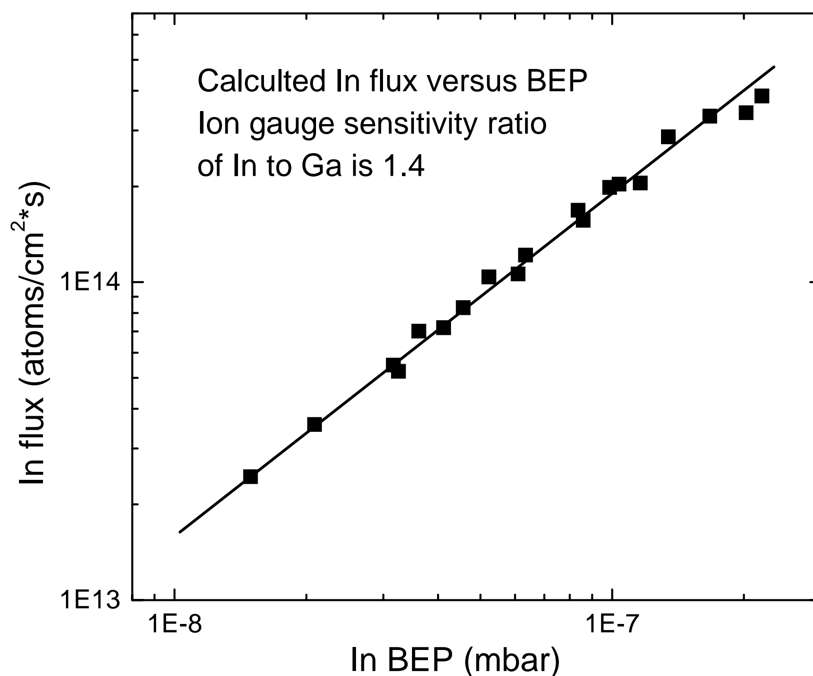

Figure 2.3 In atomic flux versus the corresponding In BEP.

2.2 X-ray diffraction

Conventional high resolution X-ray diffraction has been developed into a powerful tool for nondestructive ex-situ investigation of the epitaxial layers and structures.
The information, which is obtained from diffraction patterns, concerns the composition and uniformity of the layers, their thickness, the built-in strain and strain relaxation, and the crystalline perfection related to their dislocation density.

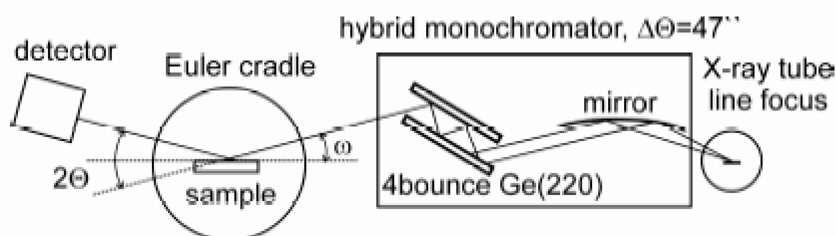

Figure 2.4 Schematic drawing of the Philips X´Pert MRD consisting of the X-ray tube, hybrid monochromator, Euler cradle and detector.

A Philips X'pert material research diffractometer was used in our experiments equipped with a copper anode (shown in Fig. 2.4). The K $_1$ radiation from the anode at a wavelength of 1.54056Å was selected for the diffraction experiments. The hybrid monochromator was composed by a graded parabolic mirror and a (220) channel-cut Germanium crystal. This Ge crystal removes the $Cu_{K\ 2}$ component from the beam. The line focus combined with the hybrid monochromator gives a low beam divergence of only 47 arcsec with high intensity. The samples are mounted onto an Euler cradle, which allows an independent variation of the incident angle ( ), the diffraction angle (2), the angle around the surface normal ( ) and the angle around an in-plane horizontal direction ( ). Measurements were performed with a 1/16° slit in front of the detector, called "double axis" configuration, which yields the resolution of 3 arcmin. High resolution (20 arcsec) was achieved in the so-called "triple axis" configuration with a secondary Ge (220) crystal monochromator in front of the detector.
The lattice spacing of the epitaxial layer grown on a substrate with known substrate constant is determined by the differentiation of Bragg's law:

$$\frac{\Delta d}{d_{hkl}} = -\frac{\Delta\theta}{\tan\theta_B} \tag{2.2}$$

where d_{hkl} is the known spacing of lattice plane with Miller indices (hkl) and $_B$ is the corresponding Bragg angle. d and are the difference of the lattice constant and the diffraction angle between the known substrates and epilayers respectively. In figure 2.5, the scattering geometry is shown. denotes the angle between the lattice plane (hkl) and the surface. k_i is the incident and k_s is the scattered wavevector.
The Bragg diffraction is called "symmetric" if = 0, i.e. the diffraction planes are parallel to the surface. For 0, the Bragg diffraction is defined as "asymmetric".

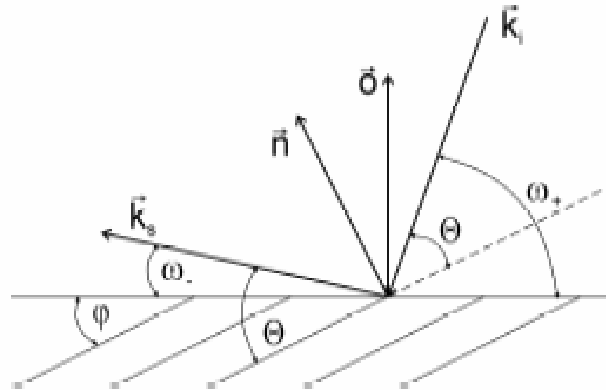

Figure 2.5: X-ray scattering geometry. $\mathbf{k_i}$: incident wavevector, $\mathbf{k_s}$: scattered wavevector, **o** : surface normal, **n** : normal on reflecting planes, : Bragg angle, : angle between surface and reflecting plane.

The linescan modes were adopted in our routine XRD measurement, i.e. " -2 scan" and " scan". For " -2 scan", the detector is rotated twice as fast and in the same direction around the diffractometer axis as the sample. In reciprocal space, this motion corresponds to change of k_s in the following way: the tip of the vector k_s moves along the reciprocal vector G_{hkl}. During the motion, the angle between the incident beam

and the sample surface changes. For asymmetric (hkl) Bragg reflections ($\omega = \theta \pm \varphi$, +: corresponds to high incidence angle and – to the low incidence) the corresponding -2 -scan direction runs also radial from the origin (000) of the reciprocal space along G_{hkl}.
In the -scan, the detector is in fixed position and the sample is rotated, i.e. . In reciprocal space, this corresponds to a path nearly perpendicular to the equivalent *-2* -scan. The scan direction is transversal in reciprocal space and thus the so-called rocking curve is obtained.
The Ewald sphere construction and reciprocal map is shown in Fig. 2.6. G_{hkl} denotes the reciprocal lattice vector and is the angle between the incident wavevector k_i and the surface plane:

$$k_s = k_i + G_{hkl} \tag{2.3}$$

In the map, for example, the rocking of around (004) is the motion of the wave vector tip in the horizontal direction. Whereas, for -2 scan, the tip of wave vector goes along (001) direction.

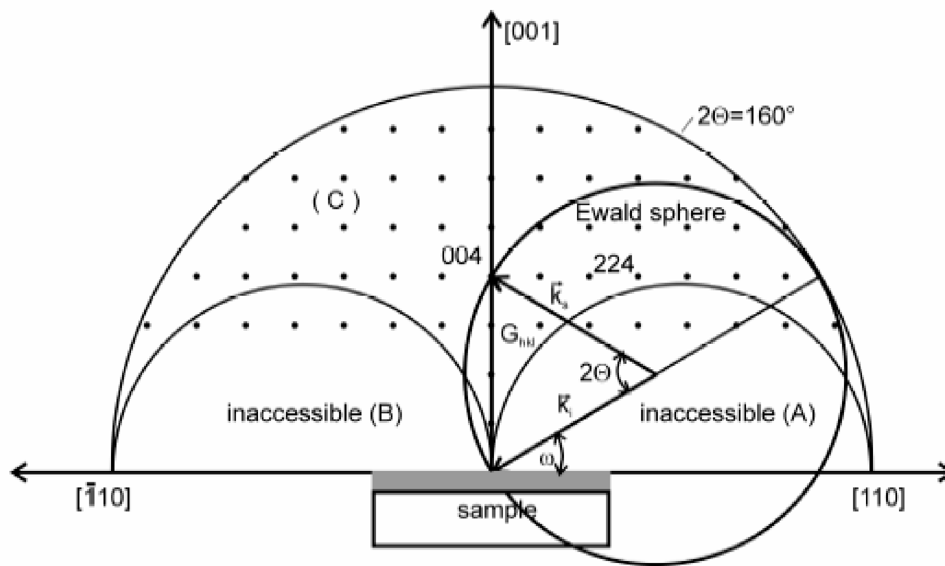

Figure 2.6 Reciprocal space map showing accessible range for Bragg reflection measurements. The radius of the outer semicircle is limited by the maximum diffractometer angle (2 = 160°). The two inner regions defined by the two semicircles are not accessible in the Bragg case.

2.3 Luminescence

Generally, luminescence refers to emission of the electromagnetic radiation due to the recombination of excess electrons and holes generated by the external excitation. The main requirement for the luminescence emission is that the system not be at

equilibrium. According to the mode of excitation, the different types of luminescence are specific in the following:

Photoluminescence (PL) —excited of excess carriers by incident photons, i.e. laser light.
Cathodoluminescence (CL) — excited by the incident electron, i.e. the electron bream in the scanning electron microscopy.
Electroluminescence (EL) — the carriers are injected through an external applied electric field.

2.3.1 Photoluminescence (PL)

PL is a routine and powerful method for characterization of direct band gap semiconductors. Through PL spectra, one can get information about the semiconductor material quality, the unintentional doping level, and the impurity energy level and so on.
The excited carriers are in non-equilibrium condition so that the carrier recombination process has to occur to reach the equilibrium with light emission. The fundamental transitions, those occurring at or near band edges are listed as follows [53]:

i. The band-to-band transition (e, h). This process is the typical interband transition that generates the intrinsic luminescence. The electrons in the conduction band directly recombine with the holes in valence band with emission of photons, which has the energy identical to the band gap of the direct semiconductor.
ii. Free exciton (X). If the material is sufficiently pure, the excited electron and hole can bind together by the Coulomb interaction into a quasi-hydrogenic exciton, which then recombine, emitting a sharp spectral line.
iii. Bound exciton. In the presence of impurities, bound exciton may be obtained. The free exciton can be localized on a neutral or ionized donor or acceptor, giving rise to the so-called exciton impurity complex. When these recombine, their emission is characterized by a narrow spectral width with lower photo energy than that of the free energy.
iv. Donor to acceptor transition (D^0, A^0). When both donor and acceptor impurities are present in the semiconductor, coulomb interaction between donor and acceptor modifies the binding energy (compared to the isolated-impurity case) such that the energy separating the paired donor and acceptor states is

$$h\nu = E_g - E_A - E_D + \frac{q^2}{\varepsilon r} \tag{2.4}$$

v. Free to bound transition. When the temperature is high enough to ionize the impurities, the low temperature donor-acceptor transition may evolve into the pure free to bound transition or spilt into two transitions, the DAP transition

and free to bound transition. The peak energy position of free to bound transition is given by

$$h\nu_p = E_g(T) - E_i + \frac{1}{2}k_B T \quad (2.5)$$

where E_i is the impurity binding energy and $\frac{1}{2}k_B T$ term results from the thermal distribution of free carriers in their bands

Our PL setup, which is shown in figure 2.7 allows the measurements of PL, as a function of the sample temperature and the excitation intensity. The luminescence is excited by the 325nm (3.815eV) line of continuous-wave He-Cd laser. A Fabry-Perot interference filter is used in order to remove the plasma line from the 325nm laser line. The laser power measured after the filter is about 4mW. The laser is then focused onto a mirror reflecting the light onto the sample fixed in the cryostat. The excited light is collected with an exit lens and dispersed in a Spex 270M monochromator equipped with a 1200 line grating and with a focal length of 27cm. The detection system consists of a GaAs photomultiplier tube and a photon counting system, controlled by a computer system. The energy resolution of this system is 0.2nm.

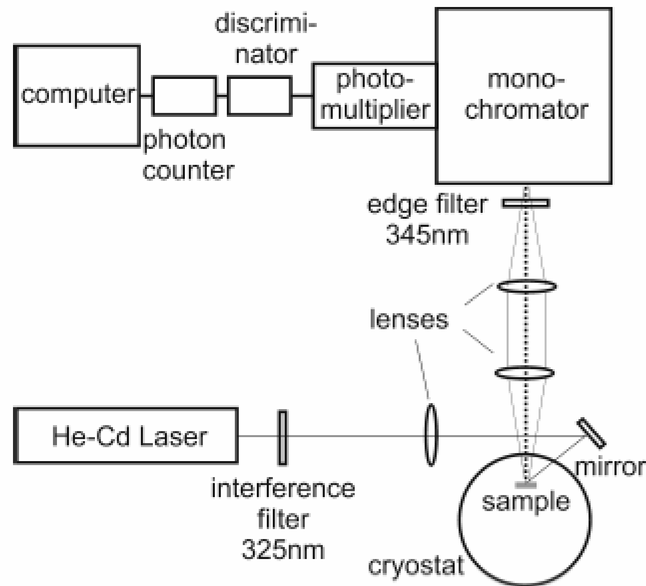

Figure 2.7 Schematic drawing of photoluminescence setup.

The cryostat allows the temperature-dependent measurement in temperature the range of 2K-300K.

2.3.2 Cathodoluminescence

The cathodoluminescence system was intensively discussed in reference[54]. A simple drawing is depicted in figure 2.8 to show our CL system. The CL is based on the Oxford CL302 light collector and a Zeiss DM950 scanning electron microscopy. The

temperature can be varied from T = 70K to room temperature. The light excited by the electron beam was collected with a parabolic mirror and coupled into a UV optical fiber connected to a 50cm Spex monochromator or focused into a R457 photomultiplier for panchromatic CL imaging with sensitivity range of 160-850nm. The light was detected by a photo counting unit controlled by the computer.

By varying acceleration voltage of the electron beam, the penetration depth can be changed to get the sample information from the position with different depth. The range of electron penetration depth was estimated by the model suggested by Kanaya and Okayama[55]. The penetration depth is expressed as:

$$R_e = \frac{0.0276 * A}{\rho * Z^{0.889}} * E_b^{1.67} (\mu m) \tag{2.6}$$

Where E_b is electron beam energy given in keV. A is the atomic weight in g/mol, and Z is the atomic number.   is the material density in g/cm^3.

In a focus mode, the excited volume can be approximated as a sphere. The vertical length of this sphere is defined as the penetration depth R_e. Defocusing the electron beam to a much larger diameter than R_e results in an excitation "cylinder" of height R_e. The values of A, Z and   for GaN and InN are listed in table 2.1.

Table 2.1 The atomic weight, atomic number and material density of GaN and InN.

parameters	A(g/mol)	Z	(g/cm^3)
GaN	83.73	38	6.06
InN	128.81	46	6.76

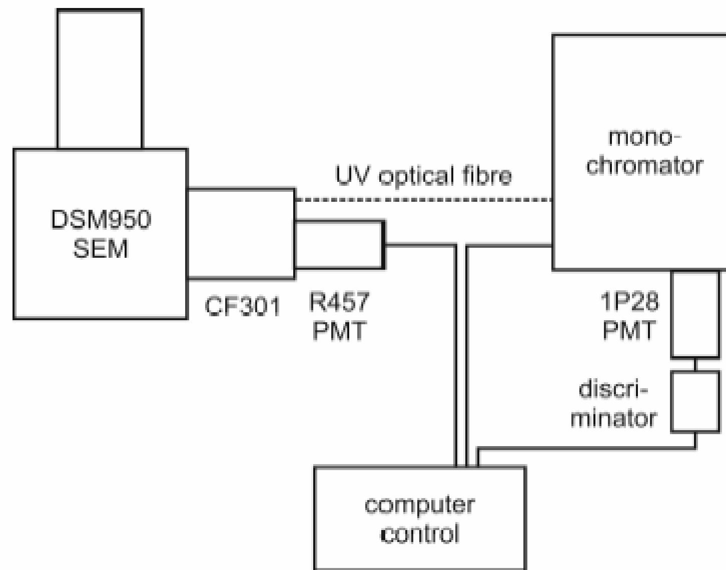

Figure 2.8 Schematic drawing of cathodoluminescence setup.

For $In_xGa_{1-x}N$, one can get the data with In mole content of x.

$$A_{In_xGa_{1-x}N} = A_{GaN} * (1 - x) + A_{InN} * x \tag{2.7}$$

$$Z_{In_xGa_{1-x}N} = Z_{GaN} * (1-x) + Z_{InN} * x \tag{2.8}$$

$$\rho_{In_xGa_{1-x}N} = \rho_{GaN} * (1-x) + \rho_{InN} * x \tag{2.9}$$

2.4 Photoluminescence excitation spectroscopy (PLE)

Photoluminescence excitation is a technique combining the properties of both PL and optical absorption. The PLE system is depicted in figure 2.9. The light source is a 1000W Xe lamp. The white light from the lamp was dispersed by the monochromator A into monochromatic light, then projected on the sample in the cryostat, where the temperature can be varied from 7K to 300K. The excited light was collected and coupled to the second monochromator, B and detected by photomultipler tube. The lock-in technology has been adopted to increase the signal-noise ratio. In PLE measurement, the excitation light wavelength is tuned by the monochromator A, and the monochromator B is set at a constant wavelength position (Normally at the position of PL peak which one is interested). The excitation light with continuously varying wavelength after monochromator A shines on the sample. When the light energy is close or above the bandgap of InGaN, the excitation light can be strongly absorbed and generate electron and hole pairs. The electrons and holes can recombine radiatively, then the intensity of luminescent light, which has the wavelength identical to the setting of monochromator B is recorded. Thus, the spectrum of the intensity of interested wavelength versus the energy of the excited light is obtained.

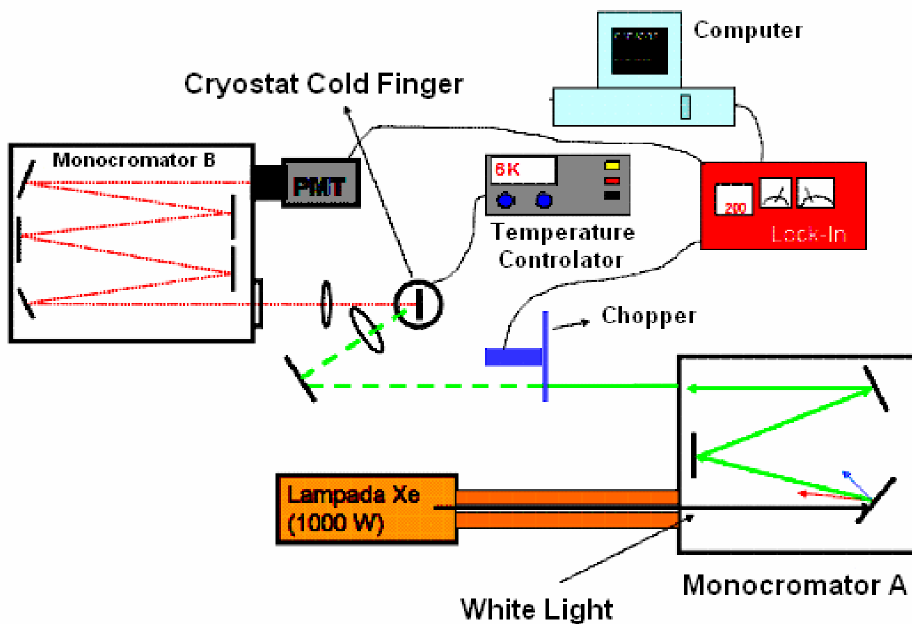

Figure 2.9 Schematic drawing of photoluminescence excitation setup.

Although the shape of the PLE spectrum mimics the shape of absorption spectrum, the

intensities of the different features do not represent actual absorption strengths. Rather, they reflect the effect that such absorption has on the recombination efficiency of the PL feature on which the analyzing spectrometer is centered. Thus, absorption in regions where recombination is very efficient could, in principle, produce features in the PLE spectrum that have considerable intensity, even in cases where the volume fraction occupied by these regions is so small as to render them undetectable by other techniques, like XRD.

3. Cubic GaN growth

3.1 Selection of substrates for cubic GaN growth

Many different kinds of substrates have been used to grow nitrides, such as sapphire [1,56], 6H-SiC [57,58], Si [46], GaN [24,59], GaAs [42,60], 3C-SiC [44,45], ZnO [61,62], r-plane Al_2O_3 [63], GaP [64], MgO [65] and $MgAl_2O_4$[66,67]. The frequently used substrates in the literature are sapphire, 6H-SiC and Si for hexagonal GaN, and GaAs and 3C-SiC for cubic GaN. The substrate data, the typical GaN quality grown on it, and the advantages and disadvantages of each substrate are summarized in Table 3.1.

3.2 Brief introduction of cubic GaN growth

In our work, we use GaAs and 3C-SiC substrates for cubic GaN MBE growth. Since the InGaN layer and structures are grown on a GaN buffer layer, the GaN quality is critical for InGaN growth. Growth of GaN has been extensively discussed in the Ph.D thesis of B. Schottker[68]. Here, only some basic knowledge about cubic GaN growth is presented.

3.2.1 Diagram of surface reconstruction transition in cubic GaN growth

The cubic GaN is a metastable phase, and is grown at slightly metal rich conditions [40]. Through well-defined stoichiometric growth conditions, high purity GaN can be obtained at proper growth temperature. Therefore, the precise control of the cubic GaN growth condition is critical to achieve high quality GaN.
In MBE c-GaN growth, the nitrogen source parameters are normally kept constant during the growth. With increasing the growth temperature, the Ga atoms sticking probability decreases. More supplied Ga is needed to compensate the enhanced desorption of Ga atoms by the increasing growth temperature. When the Ga is deficit, the surface reconstruction evolves from c(2×2) at Ga rich condition to (2×2) at N rich condition. Accompanying with that, a sharp half order streak line between the main RHEED streaks will occur.
The experiments were performed on GaAs substrate. The flux of active nitrogen atoms was calculated from the c-GaN growth rate, which is calculated from the interference fringes in reflectance measurements and the growth time. The growth temperature was elevated by the temperature calibration from the GaAs growth. Nitrogen plasma source working parameters are constant, with 130W and 0.2sccm, which gave the growth rate

of 70nm/h.

Table 3.1 Summary of substrates for hexagonal and cubic GaN growth and the results.

Substrate	Lattice constant and mismatch	Thermal expansion coefficient 10^{-6} °C^{-1}	FWHM of XRD rocking curve	Advantage (+) and disadvantage (-)
Sapphire (Al_2O_3)	*a*=0.4765nm *c*=1.300 16%	7.5 [69] (in-plane)	1.6arcmin[1] 1.9arcmin[56]	+ Stable at high temperature + Moderate cost -Large lattice mismatch -Insulating
6H-SiC	*a* = 0.3073nm *c* = 1.005nm 3.4%	4.3(a) 4.7(c) [70]	5 arcmin[58,71]	+High temperature + Conductive substrate
GaN	*a*=0.3189nm *c*=0.5186nm ~0	5.59(a) 3.17(c) [72]	3.2arcmin (0004) [59] 20 arcsec [73]	+Lattice match + High temperature - Difficult to grow
Si(111)	0.5431nm -16.9%	2.6 [74]	11 arcmin[75] 14 arcsec[76]	+ Cheap substrate + High temperature - Large difference in thermal expansion coefficient -Non-polarity
GaAs	0.56533nm -20%	5.73 [77]	20arcmin[78] 18arcmin[79]	+Easily cleaved +Polar compound +Moderate cost +Conductive -High lattice mismatch -Unstable at high temperature
3C-SiC	0.43596nm 3.7%	3.8 [32]	>14 arcmin[80,81]	+Smaller lattice mismatch +Stable at high temperature -Difficult to get high quality material

The Ga flux was measured by GaAs growth oscillations at 600°C, in which the GaAs growth was performed at V/III BEP ratio of 13, and reasonably assuming the Ga sticking coefficient of 1. The GaN growth was initiated with a 600°C grown 5nm GaN nucleation layers, followed by 720°C grown GaN layers. Then, both the growth temperature and Ga flux were varied to achieve the stiochoimetric growth condition for cubic GaN. The transition boundary of the surface reconstruction in c-GaN growth,

i.e. the relation between the growth temperature and the Ga/N ratio for stoichiometric c-GaN growth, is shown in Fig.3.1 (the original work can be found in Schikora's paper [40]).

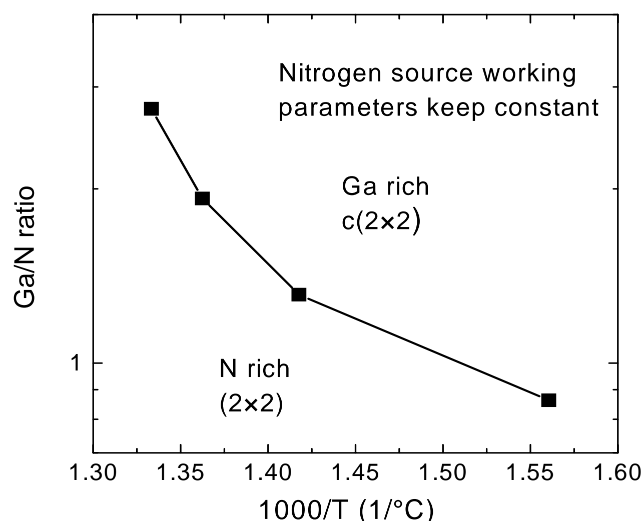

Figure 3.1 Surface reconstruction transition boundary induced by Ga/N ratio versus substrate temperature for c-GaN growth.

In stiochiometric growth condition, the Ga/N ratio decreases with the growth temperature. Apart from this line, either the metal rich or the N rich growth will occur, which will lead to surface metal droplets, rough surface, or hexagonal GaN inclusions.

3.2.2 Structural quality of c-GaN grown on 3C-SiC and GaAs substrates

In this work, two kinds of substrates, GaAs(001) and 3C-SiC(001) were used for the growth of cubic GaN. Despite the fact that 3C-SiC substrates are difficult to get, 3C-SiC substrate has some advantages over GaAs substrate. The lattice mismatch of 3C-SiC to GaN (3.7%) is much smaller than GaAs to c-GaN (20%) (table 3.1). Beside that, the 3C-SiC substrate is stable at higher growth temperature of 800°C. In the contrary, strong decomposition of GaAs substrate will occur at this temperature.
The advantages of 3C-SiC substrate deliver better quality in cubic GaN growth. Figure 3.2 shows XRD patterns on two typical GaN samples grown on 3C-SiC (#1075) and GaAs (#918), respectively. The thickness of the GaN layers were calculated from the reflectance measurements, which gave a GaN thickness of 560nm for the sample using GaAs substrate and 630nm for using 3C-SiC substrate.
Figure 3.2 (a) demonstrates the XRD -2 scans around GaN (002) reflexes on both two GaN samples on GaAs and 3C-SiC substrates. GaN Bragg peak appears around 20°. Fitting by pseudo-Voigt function gives a full width of half maximum (FWHM) of 6.5 arcmin and 9.4 arcmin for GaN on 3C-SiC and GaAs, respectively. The XRD

rocking curve of GaN Bragg peaks on these two GaN samples are depicted in Fig. 3.2 b). The X-ray rocking curve (XRC) FWHM of GaN on 3C-SiC substrate is 21.7 arcmin. For GaN on GaAs substrate, the XRC FWHM is 44 arcmin, which is significantly higher than GaN on 3C-SiC. The -2 FWHM is believed to reflect the inhomogeneous strain, the mosaic crystal size effects along the growth direction. Beside the inhomogeneous strain and mosaic crystal size effects, the dislocation density mostly influences FWHM of the rocking curve [82]. It can be seen that less dislocation density and more homogeneous layers can be obtained by using 3C-SiC substrates. The FWHM ratio of -2 scan to rocking curve is 30% for GaN on 3C-SiC and 21% for GaN on GaAs, which means the rocking curve broadening is mostly influenced by the dislocation density in the GaN layer.

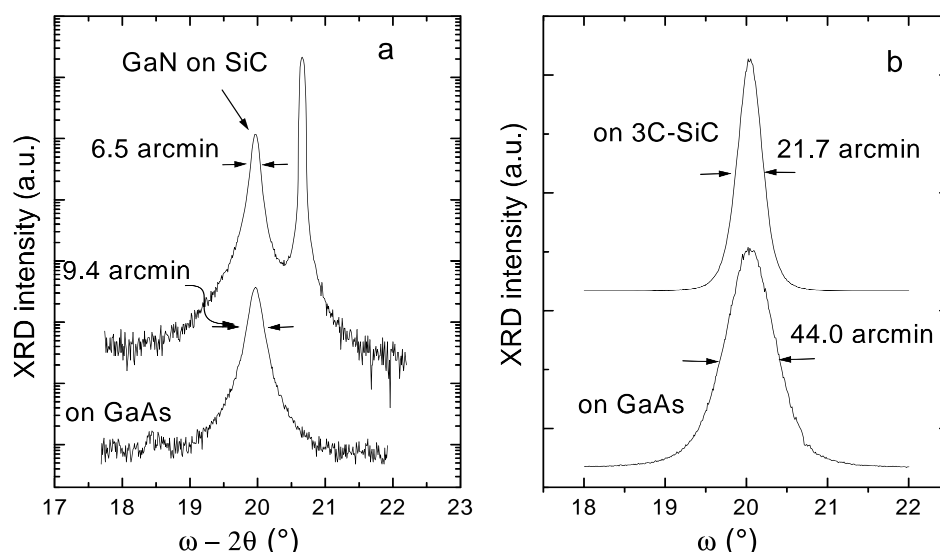

Figure 3.2 Typical HRXRD linescans on cubic GaN samples grown on GaAs and 3C-SiC substrates, respectively. a) -2 scan, b) rocking curve.

The room temperature PL spectra were also measured on these two GaN samples and plotted in Fig.3.3. The upper curve is the PL spectrum of the GaN grown on GaAs substrate, and the lower spectrum comes from GaN grown on 3C-SiC. The dominant peak at 3.2eV originates from the near band gap emission of c-GaN. The peaks at 2.1eV and 2.5eV in GaN grown on GaAs substrate are due to deep level impurities. The broad peak shoulder in the PL spectrum of GaN on 3C-SiC substrate at around 2.9 eV may come from the residual carbon impurity in the GaN layer. The linewidth of GaN emission for GaN on 3C-SiC is 66meV, which is slightly smaller than GaN on GaAs substrate (78meV). The difference in FWHM of the optical emission is much smaller than the contrast in the FWHM of X-ray rocking curve, which hints that the PL emission broadening may have a different origin from the XRD peak broadening.

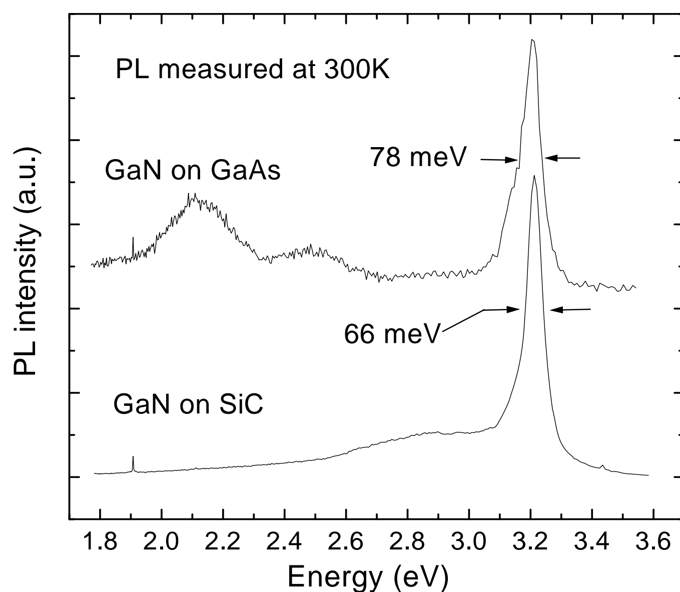

Figure 3.3 Room temperature PL spectra of GaN layers grown on GaAs and 3C-SiC substrates.

3.2.3 MOCVD growth of c-GaN

MOCVD is another important growth method for semiconductor layers. It is favored in GaN growth by its high temperature and high growth rate. Additionally, it is well known that the dislocation density in GaN decreases monotonically with increase of the layer thickness [83]. The combination of these two growth methods, MOCVD and MBE may help to get high quality thick GaN layer utilizing the advantages of both methods. In order to realize that, we performed a growth procedure as follows:

1. A thin GaN buffer was grown on GaAs substrate by MBE with a thickness of 100-450nm.
2. MOCVD epitaxy was initiated on this MBE grown c-GaN buffer layer. A thicker c-GaN layer by MOCVD growth then was obtained.
3. The MOCVD GaN thick layers then were used as buffer layers for further MBE epitaxy.

This c-GaN growth procedure allows one to take advantage of the high temperatures, and high growth rates of MOCVD with the added benefit of good surface control as seen in MBE.
A brief introduction of some experimental results will be given here. A 100 nm GaN buffer layer was initially grown by MBE. Following a 5 minute c-GaN nucleation layer growth at 570°C, the substrate temperature was risen to 720°C to grow GaN layer. This GaN layer was then put into the reactor of MOCVD equipment at University of Linz where the substrate temperature increased to 800°C at H_2 atmosphere.
From 750°C to 800°C, the NH_3 gas was delivered to the reactor for 2 minutes to etch

away a thin layer of GaN thereby exposing a fresh c-GaN surface. Then c-GaN was grown with TMGa of 8 sccm and NH_3 gas of 0.5 slm, which provided a V/III ratio of 630. A more detailed description of this growth procedure may be found in ref [84].

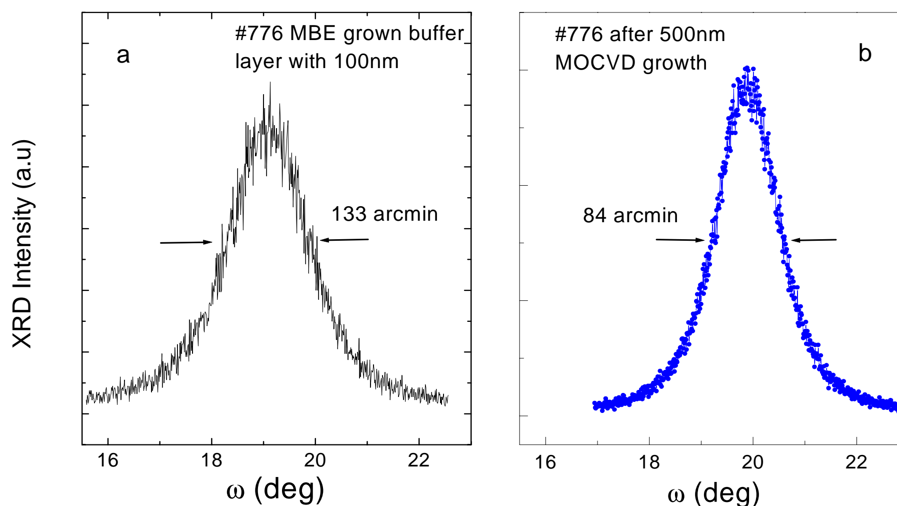

Figure 3.4 XRD rocking curves on c-GaN layers before a) and after b) MOCVD growth

In-situ optical characterization methods such as spectroscopic ellisometry and reflectometry were used to obtain growth information online. An ultra-high growth rate of 10 μm/h, which is two orders higher than MBE growth rate, was achieved and calculated from *in-situ* ellipsometry measurements. Finally a 500 nm MOCVD c-GaN layer was successfully grown on 100 nm GaN MBE buffer layer.

The HRXRD (002) rocking curves, which were measured before and after MOCVD growth are shown in Figure 3.4. The FWHM of the rocking curve decreased from 133 arcmin for 100 nm MBE c-GaN to 84 arcmin for 600 nm MOCVD c-GaN layer. The huge decrease in the FWHM signifies that the dislocation density significantly decreases due to an increasing thickness.
The rocking curve FWHM of this sample was higher than the average value from the MBE grown 600nm c-GaN layer (about 40-50 arcmin). However, after optimizing the growth, the FWHM of the c-GaN (002) rocking curve decreased to 31 arcmin (#869) with a thickness of about 1.1µm, which is in the average value of a MBE c-GaN layer of identical thickness. The growth rate for this layer, which is much lower in MBE (typically 80 nm/hr), was kept at approximately 2-3µm/h in MOCVD growth.

3.2.4 MBE growth of c-GaN on thick MOCVD c-GaN layer

We have also used MOCVD grown c-GaN layer as a substrate for MBE growth of GaN and InGaN. This MOCVD buffer layer had a thickness of 990nm.
RHEED patterns of the MOCVD growth GaN layer before MBE growth had a strongly spotty feature, indicating the rough surface of the MOCVD grown GaN layer. After the de-oxidation of the surface by the flashing Ga flux at 750°C, a 450nm MBE GaN layer

was deposited followed by a 20nm InGaN layer at 630°C.

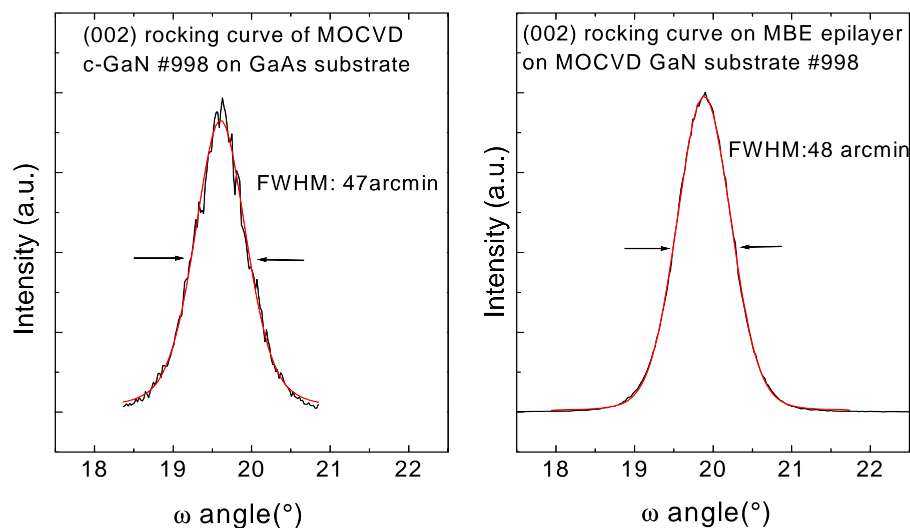

Figure 3.5 XRD rocking curve on GaN (002) reflexes of MOCVD GaN thick buffer layer and layer after MBE GaN growth on it.

At the end of MBE GaN growth, the RHEED patterns were streakier than initial readings, showing good control of surface quality by MBE growth. The XRD rocking curves of GaN by MOCVD and MBE growth are shown in figure 3.5. In the (002) rocking curve, the MOCVD grown c-GaN layer had FWHM of 47 arcmin. After MBE epitaxy on this GaN buffer, the FWHM did not decrease and kept at 48 arcmin, revealing no further decreasing of dislocation density.

The InGaN grown on this MBE/MOCVD GaN layer had comparable optical properties to the InGaN layers on the MBE grown GaN layer. All the works have demonstrated the feasibility of thick MOCVD c-GaN layers as substrates for MBE growth of c-GaN layers.

4. Growth and characterization of cubic InGaN

High quality InGaN, which acts as the active layer of the optoelectronic devices for blue, green or even yellow emission by means of tuning the indium composition, is critical for realization of high brightness LEDs and laser diodes. For this purpose, the growth and properties of InGaN based double heterostructures and quantum structures have been extensively investigated [85,1]. Although InGaN devices have been commercially realized, the growth and properties of this material still have not been well understood.

The high quality InGaN growth suffers from high volatility of In atoms, low InN binding energy, and large lattice mismatch between InGaN and GaN. Some indium related processes contribute to growth difficulties and analysis of InGaN structures, such as In segregation, InGaN phase separation and localized structure formation. Due to the metastability of the cubic III-nitrides, the c-InGaN growth has to be performed under metal-rich conditions, which further exacerbates the aforementioned problems.

The wurtzite and zinc-blende InN band gaps are still under discussion. The theoretical and experimental data of the InN band gap range from 0.6eV to 2.0eV[3]. Even with the 2.0eV of InN band gap, the InGaN with different In composition can cover the light wavelength range from red to ultraviolet. By varying the In mole fraction in InGaN layer, the highly efficient InGaN/GaN heterostructure or quantum wells can be obtained with targeted light wavelength. Some properties of hexagonal and cubic InN are listed in table 4-1.

In this chapter, after a review of InGaN growth and an introduction of other interesting topics related to InGaN, cubic InGaN growth will be discussed in detail. Also reported are results from structural and optical characterization of c-InGaN samples grown at the University of Paderborn.

4.1 Review of InGaN growth

InGaN demonstrates itself as the most mysterious material in group III-nitrides, in that many indium-induced problems makes the growth of high quality InGaN considerably difficult.

1. Low In-N binding energy. The calculated In-N binding energy is 1.93eV, which is much smaller than Ga-N (2.24eV) and Al-N binding energy (2.88eV)[39]. The weak In-N bond requires low growth temperature for In incorporation to avoid the decomposition of InGaN. From 550°C-650°C (the growth temperature used for c-InGaN MBE growth) the Indium sticking coefficient decreases from 1 to close to 0[86], which is much lower than Ga atoms in InGaN growth [87]. The cubic GaN MBE

growth temperature is about 700-750°C. In order to get significant In incorporation, the growth temperature needs to be decreased.
The low sticking coefficient of indium atoms demands high In flux for InGaN growth, which brings difficulties in controlling the stoichiometry of the InGaN growth. Indium segregation will be enhanced by high In flux, which has been proven by many researchers [88,89].

Table 4.1 Basic parameters of hexagonal and cubic InN

	InN (hexagonal)	InN (cubic)
Band gap	0.7 eV [90] 1.4 eV [91]	0.58 eV [92]
Dielectric constant (static)	15.3 , 300 K[32]	
Effective electron mass m_e	0.11m_o 300 K[93] 0.12m_o Calculated effective electron mass[94]	
Effective hole masses (heavy)m_h	1.63 m_o , 300 K[95] 0.5 m_o , calculated	
Effective hole masses (light) m_{lp}	0.27 m_o , 300 K[95] 0.17 m_o , calculated	
Lattice constant	0.3533 A (a) 300 K 0.5693 A (c) 300 K [32]	0.497nm [96]
Optical phonon energy	73 meV , 300 K [32]	
Infrared refractive index	2.9 300K [32]	2.9 300K
Thermal expansion, linear	$_a = 3.8 \cdot 10^{-6}$ °C $^{-1}$ $_c = 2.9 \cdot 10^{-6}$ °C $^{-1}$ [32]	
Piezoelectric constant	e_{31} -0.57 C m^{-2} e_{33} 0.97 C m^{-2} [97]	

However, low In flux delivers a rough InGaN surface. Both In segregation and rough surface have to be avoided by controlling the surface stoichiometry to achieve high quality InGaN structures growth.

2. Low growth temperature tends to degrade the InGaN quality due to the insufficient diffusion of the metal atoms. By compromising between crystal quality and the In incorporation, the optimal growth temperature in MBE for cubic InGaN is set around 580°C-650°C[98,51]. Another source of growth related problems is In segregation which leads to inferior interface or surface quality which deteriorates quantum well and heterostructure growth.

3. The lattice mismatch between InGaN and GaN increases with increasing In mole fraction of InGaN. When the InGaN layer is grown thicker than the critical thickness, the strain will be relieved via generation of dislocations, which degrade the device's performance. There are several models for calculation the critical thickness of the lattice mismatch system [99,100], which will be discussed in the following text. The InN

lattice constant is a useful parameter to calculate the In composition in InGaN. Unfortunately, it is still a disputed topic up to now. There are no reliable experimental data on cubic InN lattice constant. Here, we use a InN lattice constant of 0.498nm from the theoretical calculation performed by Marques [101].

4.2 Some remarkable issues of c-InGaN

The In based III-nitrides have some extraordinary optical and structural properties. Here we briefly introduce these topics and extensively ongoing discussion.

4.2.1 Alloy order and disorder

Alloy order and disordered are both common and well studied in metallic alloy. In general, the majority of III-V ternary and quaternary alloys are predicted to be thermodynamically unstable at a low growth temperature and show a tendency towards clustering and phase separation [102,103]. Thus atomic ordering is usually not expected to occur. However such a phenomenon was theoretically predicted and observed in many III-V alloys since the middle of 1980s [104,105,106,107]. In the ordered phases, the atoms can be regularly aligned in the alloy lattice at a specific composition in a short or long range, as shown in Fig.4.1

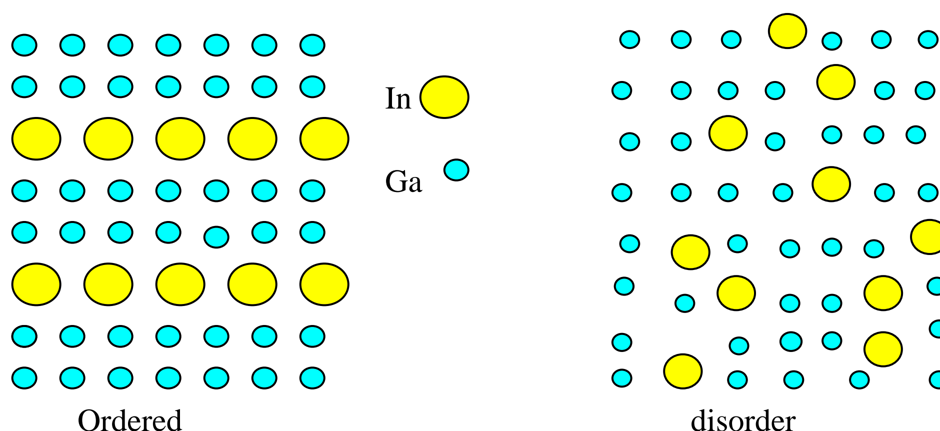

Figure 4.1 Schematic drawing of ordered and disordered phases.

The ordered phases can be detected by electron or X-ray diffraction. It shows the footprint of itself at the forbidden reflection in electron or X-ray diffraction. In the case of AlGaN, it has been shown that for some MBE growth conditions, ordering of the aluminum and gallium atoms on the metal hcp sublattice can take place [108]. It was deduced from observations of forbidden X-ray diffraction peaks in wurtzite AlGaN. Ruterana et al[109] have suggested the h-InGaN ordering phase by diffraction method in TEM. Teles et al have studied the cubic InGaN systems by combining the first-principle total energy calculations, a concentration-dependent cluster-based model and the Monte Carlo simulations. It is suggested that in the strained cubic InGaN, there are several ordered phases, which are preferentially formed in InGaN

with minus excess binding energy [110]. The ordered phase with higher In composition than the In composition around it may constitute a type of strong localized structures.

4.2.2 Phase separation

Due to the immiscibility of InN and GaN, at normally employed InGaN growth temperature, it is predicted in theory that InGaN layer with high In content will separate into two phases with different In molar contents. This is called phase separation. Phase separation is a thermodynamic equilibrium process in InGaN growth. Ho and Stringfellow [111] have investigated the miscibility gap of InGaN alloy by calculating the mixing enthalpy of InN and GaN using a modified valence-force-field model. The calculated phase diagram is shown in figure 4.2. In this figure, the solid miscibility boundary is determined by the first derivative of the mixing free energy of InN and GaN, $\partial(\Delta G)/\partial x = 0$. The spinodal points (dash line) are determined by the second derivate of ΔG, $\partial^2(\Delta G)/\partial x^2 = 0$. The bimodal line surrounds the broad immiscibility region. For example, at the growth temperature of

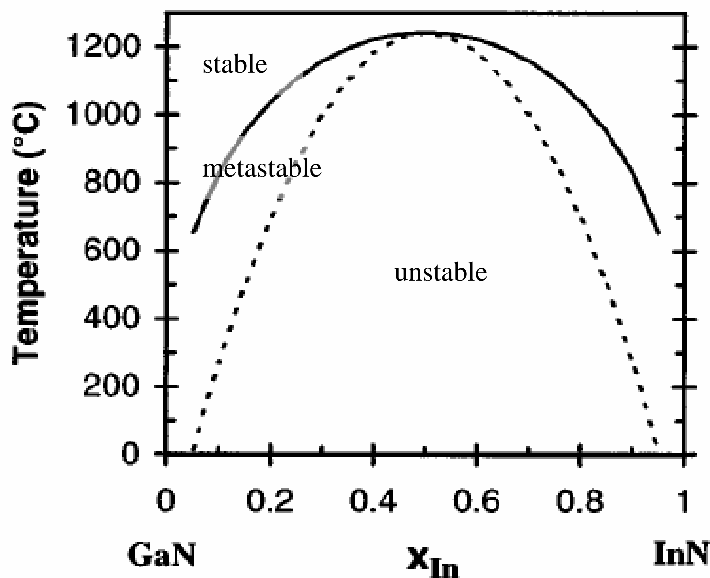

Figure 4.2 Binodal (solid) and spinodal (dashed) curves for the $Ga_{1-x}In_xN$ system, calculated assuming a constant average value for the solid phase interaction parameter. After Ho and stringfellow [111]

700°C, the alloy is immiscible in the range $0.06 \le x \le 0.94$, the alloy in this range is subjected to phase separation into the $In_{0.06}Ga_{0.94}N$ and $In_{0.94}Ga_{0.06}N$ regions in thermodynamic equilibrium. Some authors have shown some experimental evidences for the existence of phase separation in InGaN by the high resolution XRD measurement [112,113].

4.2.3 In segregation

Due to the In segregation effect, in indium based III-V compound, the ternary alloys with relative high In content may have an In content profile composed by a desired In

content layer and a higher In content surface layer. Sometimes if the In content is very high, even a floating In metal layer will appear on the surface. This is known as the In segregation effect. It is argued that the bulk binding energy difference between column III atoms is the reason for the segregation effect. Elastic strain may also play an important role in the segregation process.
In Indium based III-Nitride, this effect is related to the bond length difference of GaN, AlN, and InN (i.e. largest atoms will be pushed to surface and the In atom radius is larger than that of Ga and Al atoms). The segregation process occurs in the following way: Column III atoms, i.e. Ga atoms, impinge on the growing surface and travel sizable distances to seek a lower energy configuration. The impinging atoms can exchange with surface atoms, i.e. In atoms, by thermal process (probably at defect sites). If the segregation efficiency is high, the exchange process will repeat along the growing front. This will give a thin layer (one monolayer or less) of higher In content than in the InGaN layer. In III-nitride alloys, segregation effects will be even stronger because the binding energy difference in nitrides are higher than in the arsenides and phosphides [114].
The segregation processes was found to be very sensitive to the III/V ratio and the growth temperature [88,47]. It has strong influence on the interface due to the top $In_xGa_{1-x}N$ layer having a higher x induced by surface segregation effects.

4.2.4 Polarization fields in III-nitrides

Due to non-centro-symmetric configuration and ionic binding, the h-nitrides exhibit large piezoelectric effects under strain along the c-direction, and spontaneous polarization ($\boldsymbol{P_{sp}}$) at hetero-interfaces. The genesis of the polarization is two folds: the piezoelectric effects and the difference in spontaneous polarization between AlN, GaN, and InN even in the absence of strain.
Polarization depends on the polarity of the crystal, namely whether the bonds along the c-direction are from cation sites to anion sites or visa versa. Figure 4.3 show the polarization field in hexagonal GaN, AlGaN and InGaN. In fig.4.3 a), the crystal configuration of h-GaN, the direction of Ga cation to N anion in the bond parallel to the growth direction is the same with the z direction. This polarity is said to Ga polarity. The polarity of the crystal gives rise to an internal electric field due to the interaction between Ga cation and N anion, which is called polarization field. If the strain exists in the system, it will modify the electric field by changing the spacing between Ga plane and N plane. This strain induced additional electric field is called piezoelectric field. Shown in the fig. 4.3 b) and c) is the spontaneous and piezoelectric ($\boldsymbol{P_{pz}}$) polarization field along the growth direction in h-AlGaN and InGaN. In the contrary, zinc-blende (cubic) has symmetric configuration along growth direction of (001) (shown in Fig. 4.3 d) There is no polarization field in the growth direction.
Due to the polarization field difference in GaN and InGaN, or GaN and AlGaN, the band diagram and the carrier distribution will be influenced by these electric fields.

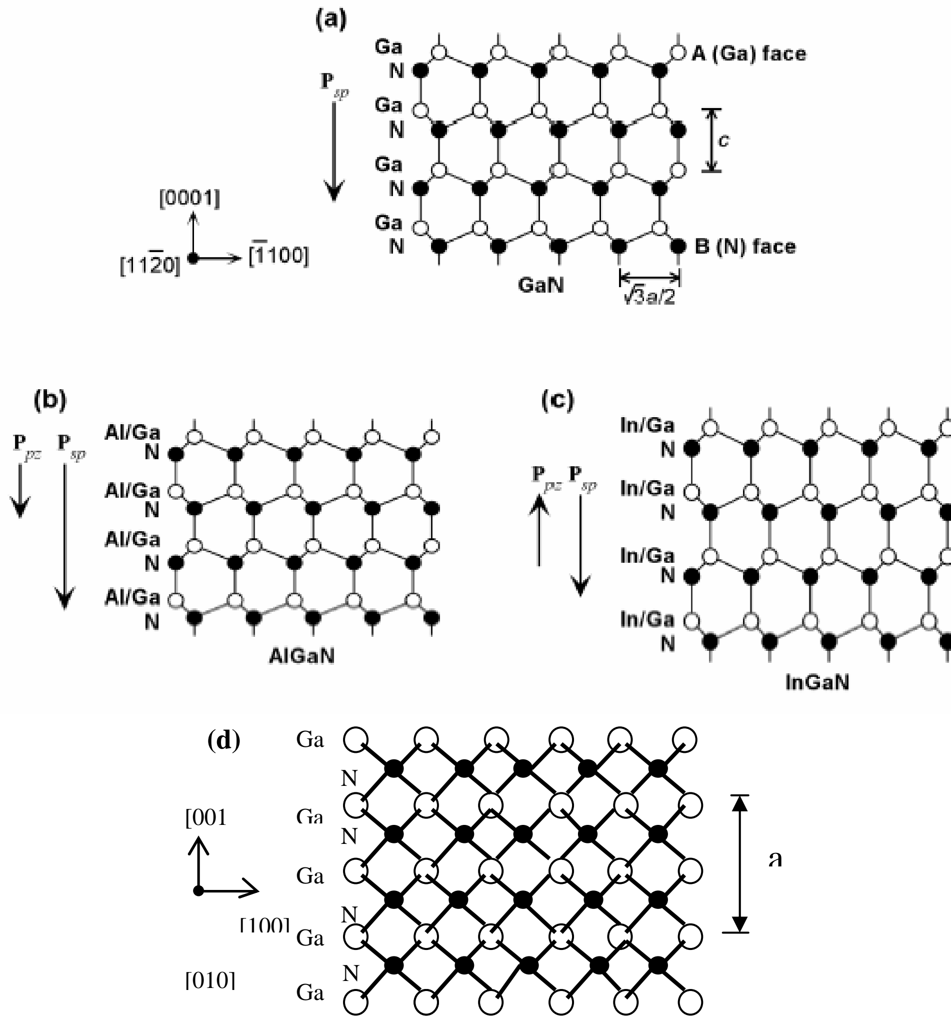

Figure 4.3 Spontaneous and piezoelectric polarization field in the III-nitride and the crystal configuration. a) h-GaN, b)h-AlGaN, c) h-InGaN. d) Non polarization field in cubic GaN.

In the case of InGaN/GaN quantum well, the band profile and carrier distribution difference in cubic and hexagonal configuration have been shown in fig. 4.4 a) and b)

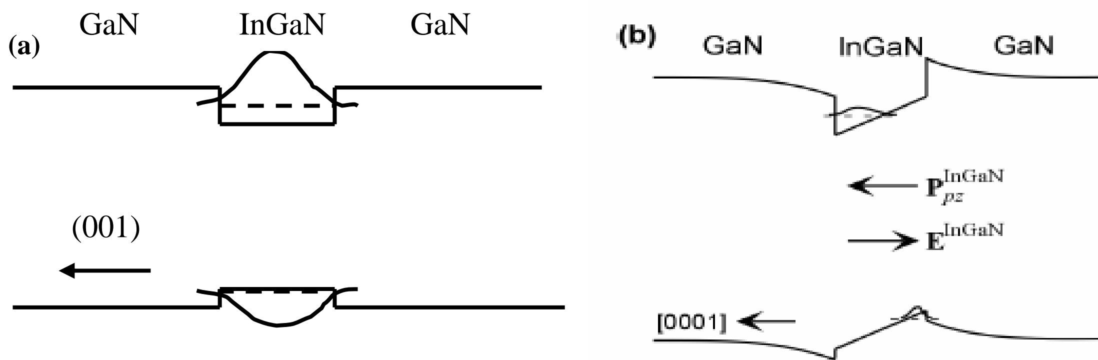

Figure 4.4 The band profile and carrier distributions in cubic and hexagonal InGaN/GaN quantum well, a) the cubic InGaN/GaN DH structure, b), the h-InGaN/GaN DH structure.

In hexagonal InGaN/GaN, the polarization field in GaN and InGaN wells results in a net electric field E^{InGaN}, which makes the tilt of the InGaN energy gap in the band profile and separates the electron and holes to the two opposite sides of the well. This gives rise to the lower transition energy of the electron from conduction band to valence band. Also, the wave-function overlap decreases with increasing the well thickness. This effect degrades the emission intensity with increasing the well thickness. Both effects are called quantum confinement Stark effect (QCSE). Bai et al have studied the variation of PL intensity with the well thickness [115]. They found that the PL intensity decreases monotonically with the well thickness. The intensity will totally quench with the well thickness above 5nm. The optimal InGaN well thickness is 2-3nm used in h-InGaN/GaN multiple quantum well growth[1,116]. Chichibu et al have shown that the polarization field is inactive in cubic polytypes by the time integrated and resolved PL measurement on cubic InGaN/GaN MQWs [26]. Therefore, one can expect that cubic III-nitrides will have a different PL intensity dependence on the well thickness, which is advantageous in the fabrication of cubic III-nitride based devices.

4.2.5 Stokes-like shift

The difference between Stokes line and Rayleigh scattering line in Raman scattering spectra is called "Stokes shift". In the optical measurement of InGaN alloys, it is frequently found that PL emission peak has a red shift to absorption edge. This shift is also defined as "Stokes shift'' or "Stokes-like shift", which has different meaning from Raman scattering measurements. This "Stokes shift'' is related to the strong localized properties of the luminescence.

There are many opinions to discuss the origin of Stokes shift. Firstly, due to the polarization field in hexagonal InGaN, the PL emission from quantum wells will have a red shift compared to the quantum well without polarization effect (as shown in Fig.4.4). The other more dominant influence on Stokes shift is the In concentration fluctuation. It is widely believed that localized structures with higher In concentration than its surrounding material are responsible for the light emission from InGaN. The excited electron and hole pairs relax to localized centers and recombine; on the other hand, the absorption edge which determines the InGaN band gap energy originates from the average band gap of the "homogenous" InGaN layer. This gives rise to the Stokes shift between the absorption and emission spectrum. In hexagonal InGaN, it is not possible to separate this spontaneous or piezoelectric polarization field from localization effects. It is believed that both of these effects will have influence on Stokes shift.

Due to the higher crystal lattice symmetry, in cubic InGaN, there exist no polarization fields in cubic InGaN. This gives a way to investigate the Stokes shift without the influence of the polarization field in cubic nitride system [117].

4.2.6 InGaN bandgap bowing and InN band gap

In the active region of the optoelectronic devices, the InGaN band gap determines the emission energy and influences the carriers confinement. Therefore, the bandgap of InGaN is an important parameter for the device performance and light emission wavelength of the In-based nitride devices. It has been suggested by some authors that the relation between the InGaN band gap and In mol content x does not follow a linear behavior[90,118], which can be fitted be polynomial function. This is called band gap bowing effect. The coefficient of the second order item in the polynomial function is called bowing parameter.
In the InGaN alloy, the InGaN PL emission is far below the InGaN bandgap. The PL emission is not an effective method to evaluate the InGaN band gap. Absorption spectrum, ellipsometry spectrum and photoluminescence excitation spectrum (PLE) measurements are widely performed to get the band gap of InGaN.
For the band gap bowing parameters, the InN band gap is a critical value, which is still under debate. The theoretical value of InN band gap in the 1990s was 2.0eV[3]. Due to the difficulty in pure InN growth, only a few data of the InN band gap of about 1.9eV [3] exist. However, Yoshimoto et al reported that the oxygen incorporation in InN will widen the band gap of InN and lead to a misinterpretation on the InN band gap data [119,120]. Wu et al have succeeded in the growth of hexagonal InN with reasonable quality. They proved that the band gap of InN is 0.7eV by different methods [121]. Using this value, they found a small band gap bowing of only b = 1.4eV. Up to now, there are still some arguments that InN band gap maybe higher than 0.7eV[122,123].
The accurate InN band gap is an important issue to clarify the InGaN band gap properties. Therefore, high quality InN is required for the measurement. Nevertheless, with any InN band gap between 0.6eV to 2.0eV, the InGaN alloy can cover the whole visible light emission range in the energy of 2.0eV to 3.0eV.

4.3 Competitive processes in InGaN growth

In InGaN growth, simultaneously several competitive processes occur. The salient rate processes involved are:

1. In incorporation into the ternary solid, "F_s" (atoms/cm^2/sec)
2. In atom desorption from the growth surface. "F_d" (atoms/cm^2/sec)
3. In incorporation as In metal droplets, " F_m" (atoms/cm^2/sec)

These action pathways are illustrated schematically in Fig. 4.5. It should be noted that rate process F_d can be due to the desorption of solitary adsorbed In atoms, or breaking of the existing In-N bond. So for an indium incident flux, F_{in} (atoms/cm^2/sec), the following mass balance equation can be assumed:

$$F_{In} = F_s + F_d + F_m \tag{4.1}$$

The incorporation of In atoms into the InGaN layer is not only been determined by the

input In flux. The growth temperature and the III-V stoichiometry on the growth front are also important to influence the In incorporation and crystal quality.
The InGaN growth temperature has the strongest impact on the sticking coefficient of indium atoms. T. Frey[51] estimated the In sticking coefficient varying from 0.1 to 0.0001 when the substrate temperature increases from 600°C to 700°C. It means In atoms has no incorporation when the growth close to 700°C. Adelmann et al[98] found that indium atoms can not be incorporated when the growth temperature is higher than 660°C.

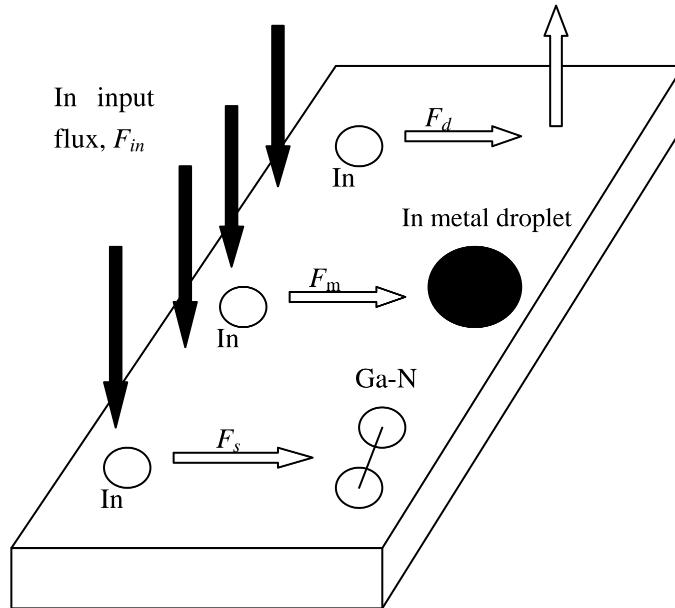

Figure 4.5 Reaction pathways for the deposition of In-based nitride compounds (after Bedair et al.1997[124]).

The high growth temperature yields a high In desorption rate and less opportunity to form In metal droplets. The desorption rate, "F_d" is inversely proportional to the residence lifetime, , of In on the growing surface where can be written as:

$$\tau = \tau_0 e^{+E_d/kT}; F_d \propto e^{-E_d/kT} \tag{4.2}$$

where $_0$ is fixed for given system and E_d is the activation energy for In desorption. The exponential temperature dependence of F_d can be dominant pathway at high growth temperature. Since the Ga atoms have a much higher sticking coefficient compared to In atoms at InGaN growth temperature, the In/Ga atoms ratio will be much smaller than that in the vapor phase. High In composition growth will require a high In flux and/or low growth temperature.

4.4 Cubic InGaN growth

In this part, the influence of In and Ga fluxes on the InGaN growth are demonstrated. After that, we will summarize the results and discuss the optimization of the InGaN growth.
Considerable efforts have been taken to optimize the growth of InGaN and obtain

in-depth understanding [125,126,127,105]. It has been found that the metal flux has a strong influence on the In-incorporation. Brandt *et al* [128] showed that In surface segregation is strongly influenced by the condition of the growth front. Nitrogen-stabilized growth yields rough interfaces of InGaN/GaN quantum wells, whereas metal-stabilized growth gives smooth interfaces and strong In segregation at the surface which leads to an increase of the well thickness. Chen *et al* [88] demonstrated the existence of stable In ad-layers on InGaN(0001) surfaces and discussed the influence of the In flux on the In incorporation. Several models were supposed to describe the In incorporation in InGaN [129,130].
As mentioned in the rate process equation 4.1, for In incorporation, the optimal In flux is critical for growing of InGaN with good optical and structural quality. There are many papers which concentrate on the In flux influence on the InGaN layer quality and interface due to the In segregation effect and In surfactant effect [88,131]
Impact of In flux on InGaN surface quality, optical and structural properties has been investigated. Both In flux and Ga flux influence on the In molar fraction x of $In_xGa_{1-x}N$ have also been studied, and a phenomenological model has been proposed to explain the x dependence on the Ga and In flux.

The GaN buffer layers were grown on 3C-SiC substrates at 700°C without a low temperature nucleation layers. Two series of InGaN layers with a thickness of about 50nm were deposited at a substrate temperature of 620°C. The first series of samples was grown at constant Ga flux of 0.036 ml/s and the In flux was varied between 0.016 ml/s and 0.1 ml/s. The second series of samples was grown with identical In flux of 0.079 ml/s and the Ga flux varying from 0.035 ml/s to 0.075 ml/s. The supplied metal fluxes and In mole fraction are shown in table 4.2. After the deposition of the InGaN layer a 35nm GaN capping layer was grown at 720°C. During all growth experiments the plasma source parameters were kept constant giving an effective N flux of 0.13 ml/s. During InGaN growth, a 5 min interruption was made after 15 min of layer growth. The growth front was monitored by *in-situ* reflection high energy electron diffraction (RHEED).

Table 4.2 Information of the c-InGaN samples for varying indium and Gallium flux.

	Ga flux (ml/s)	In flux (ml/s)	In mole fraction x
#1157	0.036	0.016	0.045
#1156	0.036	0.044	0.085
#1154	0.036	0.072	0.13
#1153	0.036	0.1	0.13
#1160	0.035	0.079	0.17
#1161	0.048	0.079	0.14
#1170	0.062	0.079	0.045
#1171	0.075	0.079	0.08

The surface of the c-InGaN layers was checked by scanning electron microscopy (SEM) and by atomic force microscopy (AFM). High-resolution X-ray diffraction